PROCEEDINGS A

royalsocietypublishing.org/journal/rspa

Cite this article: Cheng Y, Wadee MA, Málaga-Chuquitaype C. 2026 Nonlinear resonance characterization of parametrically excited pre-buckled elastic struts. *Proc. R. Soc. A* **482**: 20260072.
https://doi.org/10.1098/rspa.2026.0072

Received: 22 January 2026
Accepted: 21 April 2026

Subject Areas:
structural engineering, civil engineering, mechanical engineering

Keywords:
parametric resonance, numerical continuation, Euler–Bernoulli beam, nonlinear resonance

Author for correspondence:
Christian Málaga-Chuquitaype
e-mail: c.malaga@imperial.ac.uk

Nonlinear resonance characterization of parametrically excited pre-buckled elastic struts

Yu Cheng, M. Ahmer Wadee and Christian Málaga-Chuquitaype

Department of Civil and Environmental Engineering, Imperial College London, London SW7 AZ, UK

YC, 0009-0007-7683-2195; MAW, 0000-0001-6025-0587; CMC, 0000-0002-2538-7374

A simply supported planar elastic and inextensible strut subjected to a static axial load and a harmonic parametric excitation is studied. A variational formulation leads to a system of nonlinear partial differential equations that are subsequently discretized primarily by the first buckling mode and truncated to cubic order. Steady-state periodic responses and bifurcations are evaluated using numerical continuation and verified through finite element simulations. The analysis identifies five resonance behaviours, distinguished by their bifurcation structure, which partitions the static–dynamic loading parameter plane into regions associated with each resonance type. The present work challenges the widely accepted finding that pre-buckled inextensible struts manifest softening-type resonance under direct or parametric excitation and finds that the behaviour is richer than previous work suggests.

1. Introduction

The axially loaded elastic strut is perhaps the most studied structural instability problem [1]. Apart from its usual application as a compression member in civil, mechanical and aeronautical structures, it has more recently attracted considerable attention owing to its

Electronic supplementary material is available online at https://doi.org/10.6084/m9.figshare.c.8519930.

THE ROYAL SOCIETY PUBLISHING

inherent ability to switch elastically between a high fundamental stiffness and a low post-buckling stiffness. This feature has been demonstrated to be particularly beneficial in energy absorption, energy harvesting and vibration isolation applications [2–4], the latter involving time-dependent axial loading and the potential to experience 'parametric excitation'. The nonlinear resonance induced from such parametric excitations has been found to be advantageous for broad band-high power energy harvesting applications [5]. Recently, struts have been incorporated within metamaterial lattices [6] to facilitate the switching between high and low (or even negative) stiffnesses, which were instrumental in triggering sequential (or 'cellular') buckling [7,8] within the individual lattice cells, such that a potentially repairable energy absorbing system can be developed. Dykstra *et al.* [9] tailored metal struts into a lattice and demonstrated its efficacy in vibration suppression. Parametric instability and nonlinear oscillations of axially loaded FRP channel-section columns have also attracted increasing attention in recent years; see, for example [10]. Across these fields, a unifying theme emerges: the effectiveness of strut-based devices depends critically on their buckling-induced stiffness nonlinearity and associated nonlinear resonance behaviours.

Classical linear analyses of the axially loaded strut, culminating in the derivation of Mathieu's equation, although invaluable for delineating regions of parametric resonance [11], cannot capture amplitude-dependent frequency shifts (e.g. softening-type or hardening-type responses) or modal interactions once deflections grow. To overcome these limitations, nonlinear formulations have been developed using variational principles [12], momentum balance methods [13] or the virtual-power approach [14], ranging from approximated intuitive kinematics to those defined by the more elaborate Cosserat theory [15]. The constitutive component is typically assumed to be homogeneous and linear elastic, thus nonlinearity enters the system primarily through large curvatures and coupling among different displacement components. The resulting coupled systems of partial differential equations have been analysed through perturbation techniques [16] or modal discretization, which typically reduce the problem to Duffing–Mathieu-type equations with quadratic and cubic nonlinearities [17].

The relative importance of additional geometric effects has been discussed in [18], which demonstrates that for short and stocky struts, shear deformation becomes important as do the effects of mass moments of inertia. For sufficiently slender struts, two principal classes of struts become significant, either extensible or inextensible struts [15,19]. Extensible formulations [20] neglect axial inertia and retain stretching as the sole source of nonlinearity; they are commonly used for post-buckled struts or struts with strong axial restraints (e.g. clamped [16]) and exhibit a hardening-type resonance peak. By contrast, inextensible formulations neglect axial stretching but retain axial inertia and the geometric curvature nonlinearities associated with the elastica [12,21]; they are typically adopted for pre-buckled struts or struts with weak axial restraints (e.g. simply supported [22] and cantilever struts [23]) and generally produce softening-type frequency response functions since inertial nonlinearities dominate geometric effects. Moreover, recent studies have shown that the resonance characteristics of beam-type structures can be altered by prestressing or axial restraint; see, for instance, [24,25].

Based on inextensible formulations, previous studies on the nonlinear resonance of pre-buckled struts have primarily focused on cases where the axial load comprises a relatively small static component (P_0) and a harmonic dynamic component with amplitude P_t. For free-undamped inextensible struts under small P_0, the 'backbone curve', which describes the evolution of the natural frequency of a nonlinear system with increasing response amplitude, is typically reported to be of a softening-type. Consequently, a softening-type resonance peak is observed when the strut is subjected to direct lateral excitation [12]. In contrast, Fung [26] demonstrated that when P_0 is above 87% of the Euler load P_E, a hardening-type backbone curve is expected, as is the corresponding resonance peak under direct lateral excitation. For the case of parametric excitation, softening-type responses for $P_0 < 0.42P_E$ and $P_t < 0.21P_E$ have been reported [27], and for $P_0 = 0.5P_E$ with $P_t < 0.07P_E$ [22]. However, as far as the authors are aware, there are no studies considering the combined effects of P_0 and P_t on the overall resonance characteristics; the current aim is to address this research gap.

https://royalsocietypublishing.org/journal/rspa Proc. R. Soc. A 482: 20260072

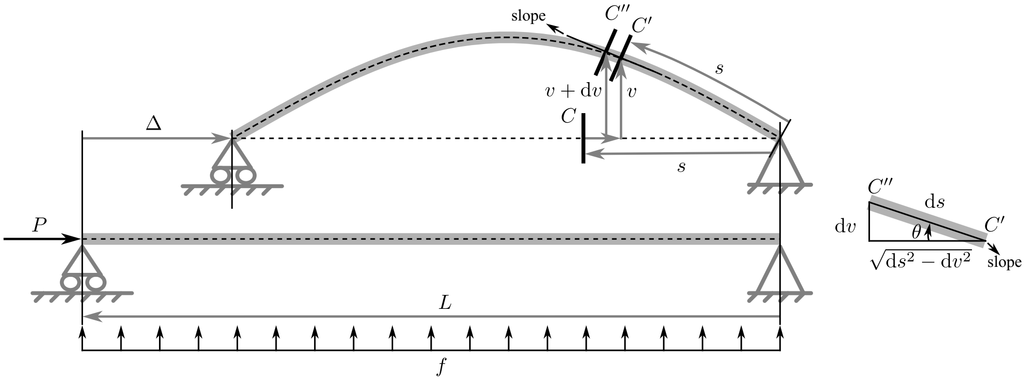

Figure 1. Simply supported strut of length L under a time-dependent axial and lateral load; flexural curvature $\kappa \equiv \theta'$.

Subsequently, the governing equations for a planar, elastic and inextensible strut are derived using variational principles and discretized primarily with the critical buckling mode, leading to a system of nonlinear ordinary differential equations (§2). The numerical solution and verification methodology is outlined in §3. Numerical continuation and path-following methods, as commonly used in nonlinear analysis (e.g. [28]) are implemented via the continuation toolbox MATCONT [29] and verified against finite element (FE) simulations conducted in ABAQUS [30]. Section 4 presents the static response and is shown to capture moderately large displacements well, while the resonance zones of the damped Mathieu's equation [31] representing the linearized system are presented. In §5, good agreement between the variational model and FE is demonstrated for both frequency–response and transmissibility functions. With the response being classified into five distinct types, an extensive study is then conducted to investigate the influence of P_0 and P_t on the behaviour of the principal parametric resonance peak. In §6a, the application of the harmonic balance method to the free-undamped system provides the backbone curve, which enables the identification of where the softening to hardening transition occurs for the resonance behaviour. The nonlinear response is further investigated through two- and three-parameter continuation of bifurcation points, including limit point bifurcations of cycles and various period-doubling bifurcations. The role of generalized period-doubling bifurcations as transition indicators between different resonance behaviours is demonstrated in §6b, and their loci are used to delineate distinct response characteristic regions within the $\tilde{P}_0$–$\tilde{P}_\mathrm{t}$ space. Conclusions are drawn in §7 where the practicalities for using buckled struts within structural isolation systems are briefly discussed.

2. Formulation

The analytical model for strut planar dynamics is formulated based on the approaches outlined in [1,13]. Figure 1 illustrates the coordinate system and displacement functions of a long, thin, inextensible strut, where s denotes the coordinate along the strut and primes indicate spatial derivatives with respect to s. An arbitrary point C when undeflected, moves to point C' when deflected, with the lateral displacement being $v(s,t)$, where t is time. The strut is assumed to be prismatic, made from a homogeneous and isotropic material with Young's modulus E, density ρ, cross-section A and second moment of area I.

The Euler–Bernoulli bending theory also assumes that the strut is rigid in shear, consequently the flexural curvature κ and end shortening Δ are given as [1]

$$\kappa = \theta' = v''(1 - v'^2)^{-1/2} \quad \text{and} \quad \Delta = -u(0,t) + \int_0^L \left(1 - \sqrt{1 - v'^2}\right) \mathrm{d}s, \tag{2.1}$$

where $u(0,t)$ denotes the axial displacement at $s=0$ and is zero for the pin end. The axial displacement function $u(s,t)$ is defined through the inextensible constraint, thus

$$u' = \sqrt{1-v'^2} - 1. \tag{2.2}$$

Since the rotational kinetic energy is negligible for a slender strut [18], only the translational kinetic energy components are considered, comprising the axial and lateral components, K_u and K_v; the strain energy of the strut comprises only the bending energy U_b—they are given thus, with the dot being used to denote differentiation with respect to time t,

$$K_u = \int_0^L \frac{1}{2}\rho A\dot{u}^2 \mathrm{d}s, \quad K_v = \int_0^L \frac{1}{2}\rho A\dot{v}^2 \mathrm{d}s, \quad U_\mathrm{b} = \int_0^L \left[\frac{1}{2}EIv''^2(1-v'^2)^{-1}\right]\mathrm{d}s. \tag{2.3}$$

A time-dependent axial load $P = P_0 + P_\mathrm{t}\cos\Omega t$ is applied at the slider end and a time-dependent uniformly distributed lateral load $f = f_0 + f_\mathrm{t}\cos\Omega t$ (unit: N/m) is applied throughout the strut length. The static axial load and lateral load intensity amplitudes are P_0 and f_0, respectively, whereas the dynamic axial load and lateral load intensity amplitudes are P_t and f_t, respectively, the dynamic forcing circular frequency is Ω, and the ratio between the axial and lateral loads is α_f, hence, $f \propto P$. Consequently, the work done by the applied loads, W_0 from the conservative loads and W_t from the non-conservative loads, are given by

$$W_0 = -P_0 u(L,t) + \int_0^L f_0 v\,\mathrm{d}s \quad \text{and} \quad W_\mathrm{t} = -P_\mathrm{t}\cos\Omega t\, u(L,t) + \int_0^L f_\mathrm{t}\cos\Omega t\, v\,\mathrm{d}s, \tag{2.4}$$

where $f_0 = \alpha_f P_0/L$ and $f_\mathrm{t} = \alpha_f P_\mathrm{t}/L$ with f providing an out-of-straightness imperfection.

Linear viscous damping is introduced to eliminate transient responses, improve numerical stability and to approximate potential sources of energy dissipation. To incorporate damping within the variational framework, the standard Rayleigh dissipation function R_d is introduced,

$$R_d = \int_0^L \frac{1}{2}c\dot{v}^2 \mathrm{d}s \quad \text{and} \quad f_\mathrm{d} = \frac{\delta R_d}{\delta \dot{v}} = c\dot{v}, \tag{2.5}$$

where c is the damping coefficient and f_d is the generalized damping force density.

The inextensibility constraint is introduced into the system through a Lagrangian multiplier $\lambda(s,t)$ [12] and its corresponding functional Λ, which is given as

$$\Lambda = \int_0^L \left\{\lambda\left[(1+u')^2 + v'^2 - 1\right]\right\}\mathrm{d}s. \tag{2.6}$$

The governing equation is obtained using the extended Hamilton's principle [14]; the stationarity of the action is augmented by the virtual work of the non-conservative forces as

$$\delta\int_{t_1}^{t_2}(\mathcal{L}+\Lambda)\,\mathrm{d}t + \int_{t_1}^{t_2}\int_0^L f_\mathrm{d}\delta v\,\mathrm{d}s\,\mathrm{d}t + \int_{t_1}^{t_2}\delta W_\mathrm{t}\,\mathrm{d}t = 0, \quad \mathcal{L} = K - \Pi = K_u + K_v - U_\mathrm{b} + W_0. \tag{2.7}$$

The variation of the combination of the action and virtual work is simplified through multiple integrations by parts yielding the following:

$$\begin{aligned}
&\delta\int_{t_1}^{t_2}(\mathcal{L}+\Lambda)\,\mathrm{d}t + \int_{t_1}^{t_2}\int_0^L f_\mathrm{d}\delta v\,\mathrm{d}s\,\mathrm{d}t + \int_{t_1}^{t_2}\delta W_\mathrm{t}\,\mathrm{d}t \\
&= \int_{t_1}^{t_2}\Bigg\{[2\lambda(1+u')\,\delta u]_0^L - P\,\delta u(L,t) + \left[\frac{EI\,v''}{1-v'^2}\,\delta v'\right]_0^L + \left[\left(-EI\left(\frac{3v''^2v'}{(1-v'^2)^2} + \frac{v'''}{1-v'^2}\right) + 2\lambda v'\right)\delta v\right]_0^L \\
&\quad + \int_0^L \left\{\left[(1+u')^2 + v'^2 - 1\right]\delta\lambda - \left[\rho A\ddot{u} + 2\lambda(1+u')'\right]\delta u\right\}\mathrm{d}s \\
&\quad - \int_0^L \left\{\rho A\ddot{v} + c\dot{v} + EI\left[\frac{v''''}{1-v'^2} + \frac{4v'''v''v'}{(1-v'^2)^2} + \frac{v''^3(1+3v'^2)}{(1-v'^2)^3}\right] - f + (2\lambda v')'\right\}\delta v\,\mathrm{d}s\Bigg\}\,\mathrm{d}t \\
&= 0.
\end{aligned} \tag{2.8}$$

https://royalsocietypublishing.org/journal/rspa Proc. R. Soc. A 482: 20260072

For the extended Hamilton's principle to hold, the terms within the temporal integral must vanish independently. The integrand of the spatial integrals (the final three terms on the right-hand side of equation (2.8)) must vanish for arbitrary δu, δv and $\delta\lambda$, which is equivalent to their multipliers vanishing, yielding, respectively, the governing equations for the axial motion and the lateral motion, alongside the inextensibility constraint. Terms with the Lagrangian multiplier λ appear within both governing equations. The two terms, $[2\lambda(1+u')]'$ and $(2\lambda v')'$, may both be considered as the internal constraint force owing to inextensibility.

The initial four terms in equation (2.8) yield the boundary conditions. Since the strut is assumed to be simply supported, the boundary conditions are thus

$$u(0,t)=0, \quad -P+2\lambda[1+u'(L,t)]=0, \quad v(0,t)=v(L,t)=0, \quad v''(0,t)=v''(L,t)=0, \tag{2.9}$$

where the second expression in equation (2.9) relates the axial force P with the boundary constraint force $2\lambda(1+u'(L,t))$ owing to the inextensibility assumption.

The governing equation of the axial motion and the boundary conditions given by equation (2.9) are incorporated into the governing equations through eliminating the Lagrangian multiplier. An example of this procedure is illustrated in [12]. The two governing equations are thus simplified into a single partial differential equation governing lateral motion as follows:

$$\begin{aligned}\rho A\ddot{v} + c\dot{v} + \rho A\frac{\mathrm{d}}{\mathrm{d}s}\left[\frac{v'}{(1-v'^2)^{1/2}}\int_s^L \ddot{u}\,\mathrm{d}s\right] \\ + EI\left[\frac{v''''}{1-v'^2} + \frac{4v'''v''v'}{(1-v'^2)^2} + \frac{v''^3(1+3v'^2)}{(1-v'^2)^3}\right] + P\frac{v''}{(1-v'^2)^{3/2}} = f,\end{aligned} \tag{2.10}$$

where

$$\ddot{u} = \frac{\mathrm{d}^2}{\mathrm{d}t^2}\left\{\int_0^s [(1-v'^2)^{1/2}-1]\mathrm{d}s\right\}. \tag{2.11}$$

The third term in equation (2.10) originates from axial kinetic energy; it contains the effect of the axial inertia given in equation (2.11) which is explicitly expressed with v and contributes to the inertial nonlinearities. The terms multiplied by EI and P, respectively, arise from the bending energy and external work done, introducing geometric nonlinearities.

The reaction force at the pin end ($s=0$) is the difference between the applied axial force and the integral of the axial inertia force of the strut. Since the definition of the sign between the axial force and axial displacement is in reverse, the reaction force R is given as

$$R = P + \int_0^L \rho A\ddot{u}\,\mathrm{d}s. \tag{2.12}$$

The following scalings are adopted to non-dimensionalize the equations:

$$\begin{aligned} & s = L\tilde{s}, \quad t = L^2\sqrt{\frac{\rho A}{EI}}\tilde{t}, \quad u = L\tilde{u}, \quad v = L\tilde{v}, \quad c = \frac{\sqrt{\rho AEI}}{L^2}\tilde{c} \\ \text{and} \quad & P = P_\mathrm{E}\tilde{P}, \quad f = \frac{P_\mathrm{E}}{L}\tilde{f}, \quad R = P_\mathrm{E}\tilde{R}, \quad \Omega = \Omega_\mathrm{n}\sqrt{1-\tilde{P}_0}\tilde{\Omega} = \Omega_{\mathrm{n},P0}\tilde{\Omega}, \end{aligned} \tag{2.13}$$

where P_E, Ω_n and $\Omega_{\mathrm{n},P0}$ are, respectively, the Euler buckling load, the natural frequency of the first linear lateral vibration mode and the preloaded natural frequency of the first linear lateral vibration mode defined as

$$P_\mathrm{E} = \frac{\pi^2 EI}{L^2}, \quad \Omega_\mathrm{n} = \frac{\pi^2}{L^2}\sqrt{\frac{EI}{\rho A}}, \quad \Omega_{\mathrm{n},P0} = \Omega_\mathrm{n}\sqrt{1-\frac{P_0}{P_\mathrm{E}}}. \tag{2.14}$$

The governing equations and the reaction force R are first non-dimensionalized with the scalings given in equation (2.13), then expanded as a power series and truncated at the cubic order, resulting in the following equations, which is typically mentioned in the literature [12,32],

$$\ddot{\tilde{v}} + \tilde{v}'''' + \pi^2\tilde{P}\tilde{v}'' + \tilde{c}\dot{\tilde{v}} + \frac{1}{2}\frac{\mathrm{d}}{\mathrm{d}\tilde{s}}\left[\tilde{v}'\int_{\tilde{s}}^{1}\frac{\mathrm{d}^2}{\mathrm{d}\tilde{t}^2}\left(\int_0^{\tilde{s}}\tilde{v}'^2\mathrm{d}\tilde{s}\right)\mathrm{d}\tilde{s}\right]$$
$$+ (\tilde{v}''''\tilde{v}'^2 + 4\tilde{v}'''\tilde{v}''\tilde{v}' + \tilde{v}''^3) + \frac{3\pi^2}{2}\tilde{P}\tilde{v}''\tilde{v}'^2 = \pi^2\tilde{f} \tag{2.15}$$

and

$$\tilde{R} = \tilde{P} - \frac{1}{2\pi^2}\int_0^1\frac{\mathrm{d}^2}{\mathrm{d}\tilde{t}^2}\left(\int_0^{\tilde{s}}\tilde{v}'^2\mathrm{d}s\right)\mathrm{d}\tilde{s}. \tag{2.16}$$

Since the initial two boundary conditions, given by equation (2.9), have already been incorporated into equation (2.10) through the elimination of the Lagrangian multiplier, only the latter two boundary conditions specified within equation (2.9) associated with v need enforcing. The system is discretized through assuming motion in its first linear buckling mode, with $\tilde{Q}(t)$ being the normalized mid-point displacement amplitude scaled with L, thus

$$\tilde{v} = \tilde{Q}(\tilde{t})\sin\pi\tilde{s}. \tag{2.17}$$

Substituting equation (2.17) into equations (2.15) and (2.16), then applying Galerkin's method to minimize the modal residuals, leads to the following ordinary differential equations (ODEs) for $\tilde{Q}(\tilde{t})$ and the normalized reaction force $\tilde{R}$,

$$\ddot{\tilde{Q}} + \tilde{c}\dot{\tilde{Q}} + \alpha_1(1-\tilde{P})\tilde{Q} + \alpha_i\tilde{Q}(\dot{\tilde{Q}}^2 + \tilde{Q}\ddot{\tilde{Q}}) + (\alpha_3 - \alpha_{3p}\tilde{P})\tilde{Q}^3 = \tilde{f} \tag{2.18}$$

and

$$\tilde{R} = \tilde{P} - \alpha_R(\tilde{Q}\ddot{\tilde{Q}} + \dot{\tilde{Q}}^2), \tag{2.19}$$

where

$$\left.\begin{aligned}&\alpha_1 = \pi^4,\quad \alpha_i = \frac{\pi^2}{48}(8\pi^2 - 9),\quad \alpha_3 = \frac{\pi^6}{2},\quad \alpha_{3p} = \frac{3\pi^6}{8},\quad \alpha_R = \frac{1}{4}\\ \text{and}\quad &\xi = \frac{\tilde{c}}{2\pi^2\sqrt{1-\tilde{P}_0}},\quad \tilde{P} = \tilde{P}_0 + \tilde{P}_\mathrm{t}\cos\left(\pi^2\sqrt{1-\tilde{P}_0}\tilde{\Omega}\tilde{t}\right),\quad \tilde{f} = 4\pi\alpha_f\tilde{P},\end{aligned}\right\} \tag{2.20}$$

with ξ being introduced as a damping ratio and α_f as a normalized imperfection measure.

3. Numerical solution and verification methodology

The vibration of the strut is subsequently analysed using the nonlinear ODE given in equation (2.18), with the cubic parametric term, $\alpha_{3p}\tilde{P}_\mathrm{t}\cos(\pi^2\sqrt{1-\tilde{P}_0}\tilde{\Omega}\tilde{t})\tilde{Q}^3$, omitted. This simplification is justified using perturbation techniques [32]; the variable is scaled with a small parameter ε, and the parametric excitation is typically associated with the ε^2 order. Consequently, the linear parametric term, $\alpha_1\tilde{P}_\mathrm{t}\cos(\pi^2\sqrt{1-\tilde{P}_0}\tilde{\Omega}\tilde{t})\tilde{Q}$, enters at the ε^3 order and is balanced by the cubic nonlinear terms. In contrast, the cubic parametric excitation term appears at the ε^5 order and would need to be balanced by quintic nonlinearities. To maintain truncation consistency, the cubic parametric term is therefore omitted.

A Nylon sample strut is considered, with a typical damping ratio of 2% [33]. Nylon is presently used as a representative benchmark for numerical verification rather than as the basis for a detailed rheological study; accordingly, it is modelled as an effective linear-elastic material with damping, which is considered to be adequate for the relatively short-duration harmonic simulations conducted herein. The direct excitation magnitude ratio is set to $\alpha_f = 5\times10^{-5}$ to ensure its effect is consistent with that of the imperfection in the FE model. Equation (2.18) is rewritten as a system of first order ODEs, transformed into an autonomous system and solved using the MATLAB [34] numerical continuation toolbox MATCONT [29]. The limit cycles are obtained using ODE45, the MATLAB's in-built fifth-order Runge–Kutta solver, over a long time (100 excitation periods) that allow transient effects to decay sufficiently. Numerical

https://royalsocietypublishing.org/journal/rspa Proc. R. Soc. A 482: 20260072

Table 1. Properties of the sample strut; note that cross-sectional area $A = bh$ and second moment of area $I = bh^3/12$.

length, L	20 mm	Young's modulus (Nylon), E	2 GPa
width, b	1 mm	density (Nylon), ρ	1150 kg m^{-3}
thickness, h	0.5 mm	damping ratio (Nylon), ξ	2%

continuation of the established limit cycles is first conducted, where a single parameter is varied while maintaining the periodic orbit. The solution stability is determined through the Floquet multipliers: if stable, all multipliers, except the trivial one, would have a magnitude under unity; if unstable, at least one multiplier would have a magnitude above unity. From the bifurcations obtained from the one-parameter continuation procedure, loci of these bifurcations are then computed through two-parameter continuation [29].

Finite element (FE) analysis is performed in parallel to verify the results from the analytical model using ABAQUS [30]. A sample strut with a rectangular cross-section is modelled, whose geometric and material properties are provided in table 1. The model employs two-dimensional, three-noded Euler–Bernoulli beam elements with cubic interpolation (element 'B23' in the ABAQUS library). A mesh convergence study is conducted, ensuring that a sufficiently fine mesh is used, resulting in a total of 20 elements along the strut. The strut incorporates an imperfection that is affine to the first buckling mode (half-sine wave) in the lateral direction. For the static buckling analysis, various mid-point magnitudes from 0.1 to 0.01 mm are adopted, as mentioned in §4a. For dynamic analysis, a mid-point magnitude of 2×10^{-4} mm, corresponding to a relative imperfection amplitude of 10^{-5} of the total length, is employed. The material is modelled as being linearly elastic and Rayleigh damping is assumed. For the static buckling analysis, the Riks arc-length method [35] is adopted to trace the load–displacement path. For dynamic analysis, an implicit dynamic procedure within ABAQUS is adopted to obtain the steady-state response of the system under specified excitation frequencies and magnitudes [36]. The 'transient fidelity' setting is selected to minimize numerical damping and ensure a suitable time increment strategy. The maximum time increment is set to 1/40 of the excitation forcing period. The total computation time is determined through trial and error (ranging from 0.1 to 2 s) for each input loading scenario and is chosen to be sufficiently large to capture the system response completely [37].

4. Preliminary analyses

(a) Nonlinear buckling

Removing all temporal and parametric excitation ($\tilde{P}_t = 0$) terms gives the equilibrium equation

$$\tilde{P}_0 = \frac{\tilde{Q}(\alpha_1 + \alpha_3\tilde{Q}^2)}{\tilde{Q}(\alpha_1 + \alpha_{3p}\tilde{Q}^2) + 4\pi\alpha_f}. \tag{4.1}$$

This is compared against FE simulations; as shown in figure 2a, the current model is shown to capture the post-buckling geometry up to $\tilde{Q} = 0.2$ (corresponding to $\tilde{P}_0 = 1.06$ and end-shortening equal to 11.3% strut length) very well. This is typically regarded as a moderately large displacement [38] and within 1% difference with respect to the FE results. For even larger displacements, the analytical model trend is similar to the FE results, but with evidence of some numerical divergence. By changing the imperfection measure, α_f, the analytical model is able to capture the effect of the global imperfection within the strut particularly in the neighbourhood of the buckling load. As shown in figure 2a, for imperfection ratios of 1/200, 1/1000 and 1/2000, the corresponding values of $\alpha_f = 1/20, 1/100$ and $1/200$ provide excellent consistency between the analytical and FE load–displacement paths.

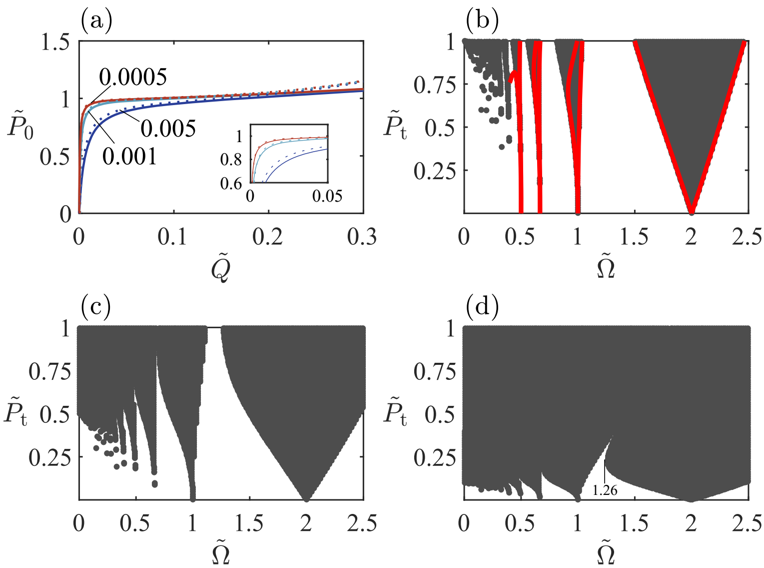

Figure 2. (a) Load–displacement function given by equation (4.1) (solid line) and FE (broken line). Different colours correspond to FE imperfection amplitudes 5/200, 1/1000, 1/2000 and corresponding to $\alpha_f = 5 \times 10^{-2}, 1 \times 10^{-2}, 5 \times 10^{-3}$; the inset diagram shows a magnified view of (a). (b) Mathieu's stability chart given by equation (4.2) with $\tilde{P}_0 = 0$ and $\xi = 0$. Black regions denote the resonance zones; red lines are the boundaries of the resonance zones reproduced from [39]; (c) is identical to (b) except $\tilde{P}_0 = 0.5$; (d) is identical to (b) except $\tilde{P}_0 = 0.9$.

(b) Damped Mathieu's equation

Removing all the nonlinear terms in equation (2.18), a damped linear system under a combination of direct and parametric excitation is obtained,

$$\ddot{\tilde{Q}} + \tilde{c}\dot{\tilde{Q}} + \alpha_1(1 - \tilde{P})\tilde{Q} = \tilde{f}. \tag{4.2}$$

The linear parametrically excited system is typically referred to as Mathieu's equation [31], while the graphical representations of the solution stability with respect to parameters are referred to as stability charts [39]. Here, the direct forcing $\tilde{f}$ has the same frequency as parametric excitation $\tilde{P}$ and has less effect on the stability of the homogeneous solution [40]; consequently, $\tilde{f}$ is neglected and the homogeneous damped Mathieu's equation is solved numerically.

With specified parameters, the solution stability is determined by the Floquet multipliers to verify whether the solution is either bounded or unbounded [39]. Collecting the corresponding parameter values of unbounded solutions and plotting those in the $\tilde{\Omega} - \tilde{P}_t$ plane yield the stability charts shown in figure 2b–d. Figure 2b shows the stability chart with zero $\tilde{P}_0$ and no damping; black regions correspond to unbounded (exponential growth) solutions, appearing around $\tilde{\Omega} = 2/k$ (k is a positive integer starting from 1) and are known as resonance zones [39]. The remaining white regions represent bounded solutions. The main two resonance zones appearing at $\tilde{\Omega} = 2$ and 1 are the principal and fundamental parametric resonance zones, respectively. The remaining thinner regions are minor parametric resonance zones for $k > 2$. The boundaries of these resonance zones are less distinct owing to numerical limitations; with a sufficiently fine numerical mesh all resonance zones would extend to lower $\tilde{P}_t$ values and attach to the abscissa. The boundaries of these resonance zones, known as transition curves, can be approximated through combined harmonic balance and perturbation techniques [39]. However, these approximations are valid only for low $\tilde{P}_t$ and k. Figure 2b shows an example where the transition curves of the initial four resonance zones are evaluated with twelfth-order power series.

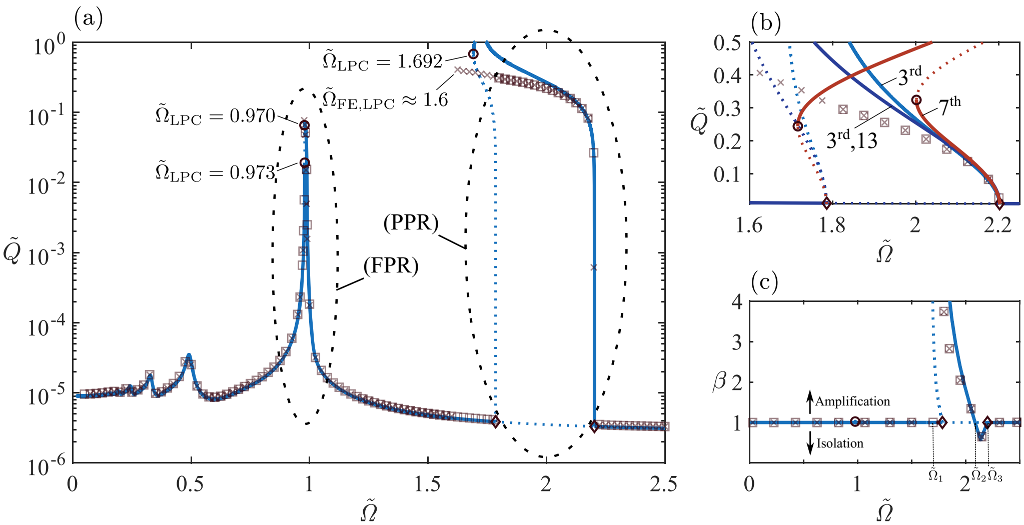

Figure 3. Frequency–response function from equation (2.18) and transmissibility with $\tilde{P}_0 = \tilde{P}_t = 0.3$. Solid and dotted lines denote stable and unstable solutions, respectively. Circle, diamond, cross and square symbols denote LPC, PD, frequency increasing (forward) sweeping FE results and frequency decreasing (backward) sweeping FE results, respectively. '3rd', '3rd, 13' and '7th' denote single-mode cubic-order, first and third mode cubic-order, single-mode seventh-order system stable solutions. (a) Maximum mid-point displacement $\tilde{Q}$ of the cubic-order system verified against FE solutions. (b) Cubic compared to higher order and multi-modal systems in the neighbourhood of $\tilde{\Omega} = 2$. (c) Reaction force magnitude transmissibility β of the cubic-order system verified against FE solutions.

The integer k denotes the resonance zone and classifies them into odd and even zones. In the odd zones, at least one Floquet multiplier is negative and thus the aperiodic responses are expected to be double the excitation period, denoted as 'period-2'. In contrast, in the even zones, the aperiodic responses have the same period as the excitation, denoted as 'period-1'. Thus, period-doubling bifurcation points would be expected around the boundaries of the odd zones for the nonlinear system; these are discussed in later sections.

Increasing $\tilde{P}_0$ expands all resonance zones, as shown in figure 2c,d. Notably, even at $\tilde{P}_0 = 0.9$, a small gap remains between the principal and fundamental resonance zones. The principal parametric resonance zone has a lower frequency boundary at $\tilde{\Omega} = 1.26$, which corresponds to the turning point of the period-doubling bifurcation locus discussed in later sections.

For the cases with damping, the resonance zones are detached from the abscissa and unstable solutions emerge only when $\tilde{P}_t$ exceeds certain thresholds. As the damping ratio ξ increases, so do the thresholds. For example, when ξ increases progressively from 0 to 2%, to 5%, and to 10%, the threshold of the principal resonance zone increases from 0 to 0.08, 0.205 and 0.399, respectively, while the fundamental resonance zone threshold increases from 0 to 0.395, 0.635 and 0.895.

5. Steady-state analysis

(a) Frequency–response function

The frequency–response function for the mid-point displacement governed by equation (2.18) under the loading scenario where $\tilde{P}_0 = \tilde{P}_t = 0.3$ is shown in figure 3a. This function comprises two parts: the period-1 main response branch occupying the whole frequency range and the period-2 principal parametric resonance (PPR) peak located around twice the natural frequency ($\tilde{\Omega} = 2$) [41]. These two branches are connected by two period-doubling (PD) bifurcation points at $\tilde{\Omega} = 1.786$ and 2.203, termed 'left' and 'right' PDs, respectively.

Table 2. Definition of the PPR peak behaviour; the curving directions are symbolized thus: (←) leftward, (→) rightward.

resonance behaviour	left branch curving direction	right branch curving direction
neutral	(→)	(←)
softening	(←) until an LPC, then (→)	(←)
hardening	(→)	(→)
neutral-hardening	(→)	(←) until an LPC, then (→)
softening–hardening	(←) until an LPC, then (→)	(←) until an LPC, then (→)

The main response branch contains the fundamental parametric resonance (FPR) peak at around the natural frequency ($\tilde{\Omega}=1$). The FPR peak corresponds to the fundamental resonance zone in Mathieu's equation. The FPR peak contains two limit point bifurcations of cycles (LPC), one near the tip at $\tilde{\Omega}=0.970$ and another one at 0.973. Although the values are close, these two LPCs indicate that the FPR peak shifts slightly to the lower frequency and exhibits a softening-type behaviour, defined as where $\tilde{\Omega}$ decreases while $\tilde{Q}$ increases.

Apart from the FPR peak, there exist some weak resonance peaks at around $\tilde{\Omega}=1/2, 1/3, 1/4$ and so on. These are the even period-1 minor parametric resonance (MPR) peaks corresponding to the even period-1 MPR zones of Mathieu's equation given in figure 2b–d. The odd MPR peaks (at $\tilde{\Omega}=2/3, 2/5$ and so on) are period-2 and do not appear under the current loading scenario. A higher $\tilde{P}_t$ value or a tighter numerical tolerance would be required for triggering or capturing respective PDs of the period-2 MPR peaks.

Next, the focus is upon the PPR peak. On the main response branch, the left and right PDs appear as the transition from a stable to an unstable solution and interconnected with a period-1 unstable solution branch. A period-2 solution branch bifurcates from both PDs, constructing the PPR peak. Owing to the adopted linear viscous damping, the curve is difficult to compute in a complete form and is therefore presented as two separated branches starting from two PDs, respectively. The inclusion of cubic damping [42] or an end axial dashpot, which can generate a Van der Pol oscillator-type nonlinear damping [22], would be able to merge the separated branches at a reasonable computation cost, but this is left for future work.

The branches emanating from the left and right PDs are referred to as the left and right branches of the PPR peak, respectively. The left branch curves towards lower frequencies and initially consists of an unstable solution segment, which restabilizes after reaching an LPC at $\tilde{\Omega}=1.692$. The right branch also curves towards lower frequencies but contains only stable solutions. Consequently, the left and right PDs are subcritical and supercritical, respectively. The criticality of these two PDs is also shown by the Poincaré maps and bifurcation diagram presented in §S3 of the electronic supplementary material. Since the complete solution structure is not available, the analysis primarily focuses on the local response behaviour of the PPR peak within the range $\tilde{Q}<0.5$. Physically, this upper bound corresponds to the mid-point displacement of the strut not exceeding half of its length ($\tilde{Q}=0.5$), which is, in fact, a huge deflection.

Five distinct types of resonance behaviour are encountered currently: three basic types, (i.e. softening, neutral and hardening) and two composite types (i.e. neutral–hardening and softening–hardening). The behaviour of a PPR peak is classified according to the tendencies of its left and right branches, as summarized in table 2, where curving rightward (→) denotes the branch extending towards a higher frequency while curving leftward (←) denotes extending towards a lower frequency. Consequently, under the current loading scenario, $\tilde{P}_0=\tilde{P}_t=0.3$, the PPR peak exhibits softening behaviour.

The FE results for the sample strut under the same loading scenario are also presented in figure 3a. The comparison between the analytical and FE results is generally excellent; however, when $\tilde{Q}>0.2$, the analytical model tends to overestimate the response as also shown in figure 3a. Moreover, the 'backward' FE solutions, i.e. those obtained by sweeping the excitation frequency from high to low values, suggest that the softening behaviour should persist with a large amplitude response and extend to lower frequencies, down to $\tilde{\Omega} \approx 1.6$. In contrast, the current analytical model exhibits a comparatively gentler softening response and predicts a loss of the softening characteristic at higher $\tilde{Q}$ values.

Including the higher-order terms within the equation while maintaining the single mode discretization does not improve the consistency with the FE results at very large displacements, as shown in figure 3b. The reason being that when the response amplitude is large, where $\tilde{Q} = (0.3, 0.4)$, the assumed single half-sine wave mode for the analytical model becomes less accurate in describing the deformation shape of the strut. Introducing higher symmetric linear modes in the discretization (for example, including the first and third modes with a cubic-order truncation, as shown in figure 3b) is able to improve the comparison with the FE results at larger deformations; however, the modest improvement is counterbalanced by the significantly increased system complexity and computation cost. A comparison between the full inextensible model and a reduced model retaining only geometric nonlinearities is presented in §S4 of the electronic supplementary material. Under identical loading conditions ($\tilde{P}_0 = \tilde{P}_t = 0.3$), the full inextensible model exhibits a softening-type response, consistent with the FE results, whereas the reduced model displays a hardening-type response. This clear discrepancy underscores the dominant role of inertial nonlinearity in determining the characteristics of the resonance peak.

(b) Transmissibility function

With the periodic solutions of $\tilde{Q}$, $\dot{\tilde{Q}}$ and $\ddot{\tilde{Q}}$ obtained through the described numerical continuation procedure, the corresponding periodic response force $\tilde{R}$ is computed from equation (2.19). The magnitude ratio transmissibility, denoted as β, is defined as

$$\beta = \frac{\max(\tilde{R}) - \min(\tilde{R})}{2\tilde{P}_t}, \tag{5.1}$$

where $\max(\tilde{R})$ and $\min(\tilde{R})$ represent the upper and lower bounds of $\tilde{R}$, respectively. The graph of β varying with $\tilde{\Omega}$ is shown in figure 3c for the loading scenario $\tilde{P}_0 = \tilde{P}_t = 0.3$.

In the neighbourhood of the PPR frequency, the response force may exceed or fall below the excitation force, corresponding to amplification ($\beta > 1$) or isolation ($\beta < 1$), respectively. Amplification occurs between the LPC at $\tilde{\Omega}_1 = 1.692$ and the isolation frequency $\tilde{\Omega}_2 = 2.088$, while isolation is subsequently observed between $\tilde{\Omega}_2$ and the PD at $\tilde{\Omega}_3 = 2.203$. The transmissibility curve exhibits a softening-type characteristic, consistent with the mid-point displacement response. A smaller amplification region is also observed near the FPR frequency, $\tilde{\Omega} = [0.978, 1.002]$, with a relatively modest effect. Overall, there is good agreement between the analytical and FE results, except in regions where $\beta > 4$. Such discrepancies are also seen in the mid-point displacement and are attributed to the limitations of the single-mode discretization used in the analytical model. Notably, amplification and isolation are observed only near the FPR and PPR frequencies and within a limited frequency band, where the axial inertia force becomes comparable to the applied axial excitation. Unlike amplification, the isolation effect is minimal for the present pre-buckled ($\tilde{P}_0 < 1$) scenario, but is expected to be more pronounced in the post-buckled case, which is left for a future investigation.

6. Parametric studies

(a) Natural frequency and backbone curve

The free-undamped system ($\xi = 0$, $\tilde{P}_t = 0$) is analysed using the single-harmonic balance method to determine the amplitude-dependent natural frequency and the influence of $\tilde{P}_0$. The natural frequency represents the vibration frequency of a conservative system under a perturbation. In the linear case, the natural frequency is constant, reflecting the invariance of the total energy. In contrast, a nonlinear system exhibits an amplitude-dependent—therefore an energy-dependent—natural frequency. The vibration amplitude acts as a correction to the linear natural frequency; the resulting functional relationship between amplitude and frequency is typically referred to as the backbone curve. For small amplitudes, the correction is negligible, and the natural frequency coincides with that of the linear system. However, as the amplitude grows sufficiently large, the frequency deviates significantly from its linear value. A positive correlation between amplitude and frequency yields a hardening-type backbone curve, which manifests as a right-leaning resonance peak under direct excitation, while a negative correlation indicates a softening-type backbone curve that leans in the opposite direction [21].

Removing the damping and excitation terms reduces equation (2.18) to

$$\ddot{\tilde{Q}} + \pi^4(1-\tilde{P}_0)\tilde{Q} + \frac{\pi^6}{2}\left(1-\frac{3\tilde{P}_0}{4}\right)\tilde{Q}^3 + \frac{\pi^2(8\pi^2-9)}{48}\tilde{Q}(\dot{\tilde{Q}}^2+\tilde{Q}\ddot{\tilde{Q}}) = 0. \tag{6.1}$$

The single harmonic balance method is adopted and the solution is assumed to be

$$\tilde{Q} = \tilde{q}\sin(\omega t) = \tilde{q}\sin(\pi^2\sqrt{1-\tilde{P}_0}\,\tilde{\omega}\tilde{t}), \tag{6.2}$$

where $\tilde{q}$ is the normalized amplitude and ω is the amplitude-dependent natural frequency. Substituting this assumed solution into equation (6.1) yields

$$\begin{aligned}&\left[-\tilde{\omega}^2\tilde{q} + \tilde{q} + \frac{3\pi^2}{8}\left(\frac{1-3\tilde{P}_0/4}{1-\tilde{P}_0}\right)\tilde{q}^3 - \frac{\pi^2(8\pi^2-9)}{96}\tilde{\omega}^2\tilde{q}^3\right]\sin(\pi^2\sqrt{1-\tilde{P}_0}\tilde{\omega}\tilde{t})\\ &\quad+\left[-\frac{\pi^2}{8}\left(\frac{1-3\tilde{P}_0/4}{1-\tilde{P}_0}\right)\tilde{q}^3 + \frac{\pi^2(8\pi^2-9)}{96}\tilde{\omega}^2\tilde{q}^3\right]\sin(3\pi^2\sqrt{1-\tilde{P}_0}\tilde{\omega}\tilde{t}) = 0.\end{aligned} \tag{6.3}$$

Through applying Galerkin's method, the higher harmonic term, i.e. the term with $\sin(3\pi^2\sqrt{1-\tilde{P}_0}\tilde{\omega}\tilde{t})$ vanishes, leaving only the coefficient of $\sin(\pi^2\sqrt{1-\tilde{P}_0}\tilde{\omega}\tilde{t})$, allowing $\tilde{\omega}$ to be expressed in terms of $\tilde{q}$. Expanding this expression as a power series in $\tilde{q}$ and retaining the first nonlinear term gives the following approximate solution:

$$\tilde{\omega}^2 \approx 1 + \frac{3\pi^2}{8}\left[\frac{1-3\tilde{P}_0/4}{1-\tilde{P}_0} - \frac{8\pi^2-9}{36}\right]\tilde{q}^2 = \tilde{\omega}_0 + \tilde{\omega}_2\tilde{q}^2, \tag{6.4}$$

where $\tilde{\omega}_0$ is the linear natural frequency, which is unity owing to the adopted non-dimensionalization defined in equation (2.13), and $\tilde{\omega}_2$ is the coefficient of the quadratic amplitude term acting as a corrector on $\tilde{\omega}_0$. Note that $\tilde{\omega}_2 = 0$ when $\tilde{P}_0 = \tilde{P}_{0,\mathrm{n}} = (8\pi^2-45)/(8\pi^2-36) \approx 0.791$.

Figure 4a shows the relationship between $\tilde{\omega}_2$ and $\tilde{P}_0$. When $\tilde{P}_0 = 0$, $\tilde{\omega}_2 = -3.491$, implying the reduction of $\tilde{\omega}$ as $\tilde{q}$ increases, which corresponds to the softening-type backbone curve as shown in figure 4b. Reducing $\tilde{P}_0$ causes an increase in $|\tilde{\omega}_2|$; the backbone curve has a higher curvature towards lower frequencies implying an enhancement of softening behaviour. On the contrary, while increasing $\tilde{P}_0$ values but below $\tilde{P}_{0,\mathrm{n}}$, $\tilde{\omega}_2$ remains negative but decreases in magnitude, and the curvature of the backbone curve becomes small. At $\tilde{P}_{0,\mathrm{n}}$, $\tilde{\omega}_2 = 0$ and thus $\tilde{\omega} = \tilde{\omega}_0$, implying that, under quadratic truncation of $\tilde{\omega}$, the nonlinearity shows no effect on the system and the backbone curve becomes a vertical line. When $\tilde{P}_0 > \tilde{P}_{0,\mathrm{n}}$, $\tilde{\omega}_2$ becomes positive, and its magnitude increases with $\tilde{P}_0$, suggesting that a hardening-type backbone curve emerges, becoming more pronounced as $\tilde{P}_0$ increases further. When $\tilde{P}_0$ approaches unity, $\tilde{\omega}_2$ blows up, because the preloaded natural frequency $\Omega_{\mathrm{n},P0}$, given in equation (2.14), vanishes and becomes unsuitable as a non-dimensionalization parameter. Moreover, at the buckling load, the natural frequency becomes completely dependent on the nonlinearities.

Section S1 of the electronic supplementary material presents the frequency–response functions of the directly excited nonlinear system for different values of $\tilde{P}_0$ and direct excitation amplitude $\tilde{f}_\mathrm{t}$. The results indicate that the excitation amplitude has a relatively minor influence on the characteristics of the resonance peak. Moreover, the backbone curve provides a generally reliable prediction of the resonance behaviour, although the predicted transition value exhibits a slight discrepancy that can be reduced by incorporating additional harmonics and higher-order nonlinear terms in the backbone curve approximation.

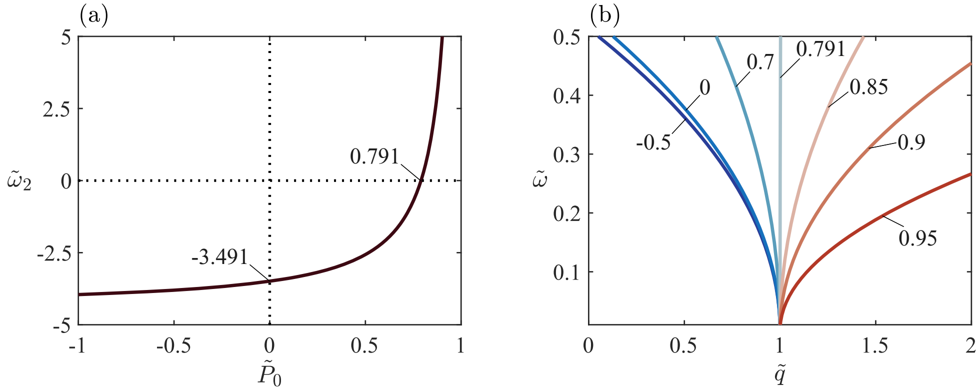

Figure 4. The quadratic corrector and backbone curve. (a) Effect of $\tilde{P}_0$ on the coefficient of the quadratic term, $\tilde{\omega}_2$. (b) Backbone curve of $\tilde{\omega}$ with different colours denoting different $\tilde{P}_0$.

(b) Loading parameter effects on principal parametric resonance peak

Analysis of the free-undamped system identified a transition $\tilde{P}_0$ value marking the change between softening and hardening behaviour. For a directly excited nonlinear system, the excitation amplitude has less influence on the trend of the resonance peak. In this case, the peak closely follows the backbone curve, and the resonance behaviour is governed solely by $\tilde{P}_0$. In contrast, for a parametrically excited system, the excitation amplitude $\tilde{P}_t$ also affects the resonance behaviour and acts in combination with $\tilde{P}_0$. The influence of these parameters on the characteristics of the PPR peak is studied currently through numerical continuation.

(i) Effect of $\tilde{P}_t$ on frequency–response function

The influence of $\tilde{P}_t$ on the PPR resonance peak is first examined by varying its magnitude while keeping $\tilde{P}_0$ fixed. Figure 5a,b shows the evolution of the PPR resonance peak for $\tilde{P}_0 = 0.3$ as $\tilde{P}_t$ increases; the resonance peak is observed to broaden, as indicated by the growing frequency separation between the two PDs. For $\tilde{P}_t = 0.4$, the response is softening-type according to the definitions given in table 2. An LPC emerges on the left branch connecting with the subcritical left PD with an unstable solution segment, while the right PD is supercritical. When $\tilde{P}_t$ is increased to 0.5, the PPR peak continues to exhibit a softening-type response, but the LPC moves towards the left PD: $\tilde{Q}$ decreases from 0.482 to 0.218, and the frequency difference between the LPC and the left PD, $\Delta\tilde{\Omega}$, decreases from 0.04 to 0.003. This reduction in $\Delta\tilde{\Omega}$ reflects the shrinking frequency interval over which two stable and one unstable solutions coexist, indicating a reduction of the softening effect. As $\tilde{P}_t$ is increased further to 0.6, the response becomes neutral-type, with the LPC and its associated unstable segment on the left branch disappearing, leaving only stable branches emanating from both PDs, which are both supercritical.

Further increasing $\tilde{P}_t$ from 1.0 to 1.1 and 1.2 leads to a transition back from neutral-type to softening-type behaviour. At $\tilde{P}_t = 1.1$, an LPC and its associated unstable segment re-emerge on the left branch, and the left PD becomes subcritical once again. Increasing $\tilde{P}_t$ from 1.1 to 1.2 causes the LPC to move away from the left PD, with $\tilde{Q}$ increasing from 0.085 to 0.127 and $\Delta\tilde{\Omega}$ increasing from 0.002 to 0.008. This indicates an expansion of the frequency interval over which two stable and one unstable solutions coexist, signifying softening behaviour enhancement.

Figure 5c,d presents the corresponding results for $\tilde{P}_0 = 0.85$. As $\tilde{P}_t$ increases, the resonance peak broadens, reflected by the growing frequency separation between the two PDs. The right PD frequency increases monotonically with $\tilde{P}_t$, whereas the left PD frequency decreases as $\tilde{P}_t$ increases from 0.04 to 0.35, before reversing and increasing again for $\tilde{P}_t = 0.4$ and 0.45, which is referred to as a 'U-turn' of the left PD.

For $\tilde{P}_t = 0.04$, the response is of a hardening-type. The right branch emanates from a subcritical right PD and is entirely unstable. A (hardening) LPC is located at unrealistically large response

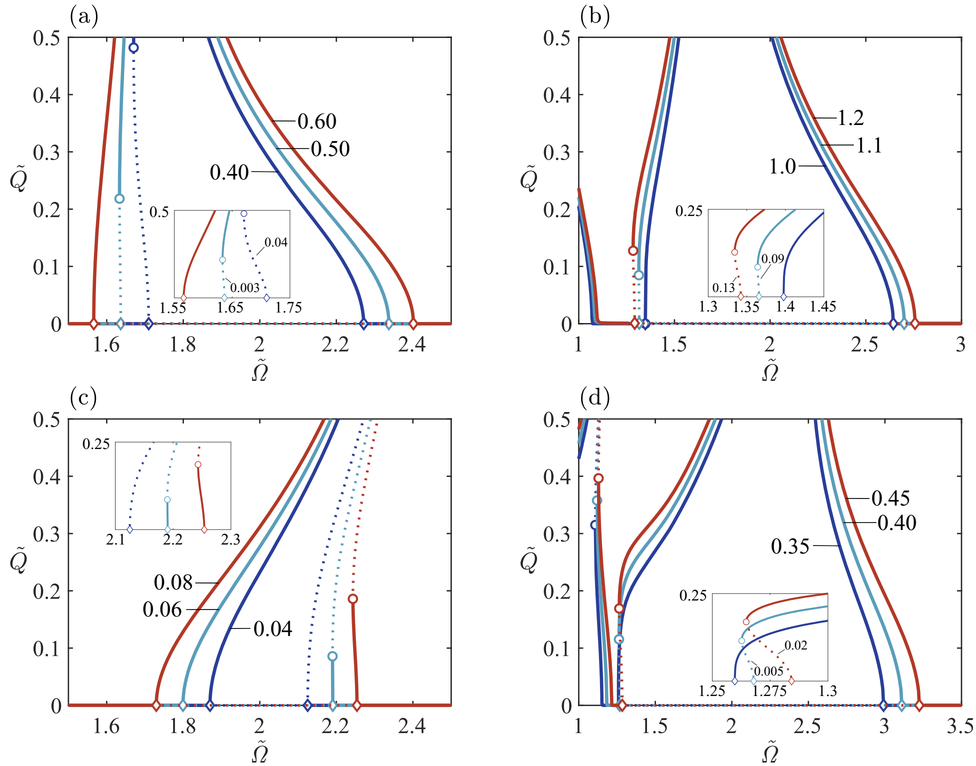

Figure 5. Frequency–response function of equation (2.18) in the neighbourhood of $\tilde{\Omega} = 2$ with various $\tilde{P}_{\rm t}$ values. Solid and dotted lines denote stable and unstable solution parts, respectively. Symbols: '○' and '◇' correspond to LPC and PD, respectively. (a) $\tilde{P}_0 = 0.30, \tilde{P}_{\rm t} = \{0.40, 0.50, 0.60\}$; (b) $\tilde{P}_0 = 0.30, \tilde{P}_{\rm t} = \{1.0, 1.1, 1.2\}$; (c) $\tilde{P}_0 = 0.85, \tilde{P}_{\rm t} = \{0.04, 0.06, 0.08\}$; (d) $\tilde{P}_0 = 0.85$, $\tilde{P}_{\rm t} = \{0.35, 0.40, 0.45\}$; the inset diagrams show a zoomed-in view of the corresponding diagrams; the arrowed-out numbers in the inset diagrams are $\Delta\tilde{\Omega}$.

amplitudes (i.e. $\tilde{Q} > 1$), near the tip of the PPR peak and at a frequency higher than the right PD, and connects this right branch to the stable left branch, which bifurcates from a supercritical left PD. As $\tilde{P}_{\rm t}$ increases to 0.06, the response transitions to neutral–hardening-type. The right PD becomes supercritical, and the right branch is stable up to a newly emerged (neutral) LPC, beyond which it becomes unstable. Two LPCs are now present on the right branch of the PPR peak: the neutral LPC, visible within the $\tilde{Q} < 0.5$ range, and the hardening LPC located near the tip of the resonance peak. Increasing $\tilde{P}_{\rm t}$ to 0.08 and further to 0.35 preserves the neutral-hardening-type behaviour. During this range, the neutral LPC moves progressively away from the right PD: $\tilde{Q}$ increases from 0.086 to 0.186 and then to 0.849 (beyond the $\tilde{Q} < 0.5$ range), while $\Delta\tilde{\Omega}$ between the neutral LPC and the right PD increases from 0.001 to 0.011 and 0.49, respectively.

Further increasing $\tilde{P}_{\rm t}$ from 0.35 to 0.4 and 0.45 leads to a transition from neutral-hardening-type to softening–hardening-type behaviour. It is noteworthy that for large $\tilde{P}_0$ and $\tilde{P}_{\rm t}$, the FPR and PPR peaks broaden and approach each other, although no direct interaction between the two peaks is observed within the pre-buckled $\tilde{P}_0$ range. At $\tilde{P}_{\rm t} = 0.4$, a new (softening) LPC appears on the left branch, connecting to the subcritical left PD through an unstable solution segment. Three LPCs are now present: the softening LPC on the left branch, within the $\tilde{Q} < 0.5$ range, the neutral LPC on the right branch and the hardening LPC at the tip of the resonance peak, with the latter two occurring at large $\tilde{Q}$. Increasing $\tilde{P}_{\rm t}$ from 0.4 to 0.45 causes the softening LPC to move away from the left PD ($\tilde{Q}$ increases from 0.115 to 0.169 and $\Delta\tilde{\Omega}$ from 0.005 to 0.02), while the neutral LPC simultaneously moves away from the right PD ($\tilde{Q}$ increases from 0.977 to 1.116 and $\Delta\tilde{\Omega}$ from 0.593 to 0.695).

https://royalsocietypublishing.org/journal/rspa Proc. R. Soc. A 482: 20260072

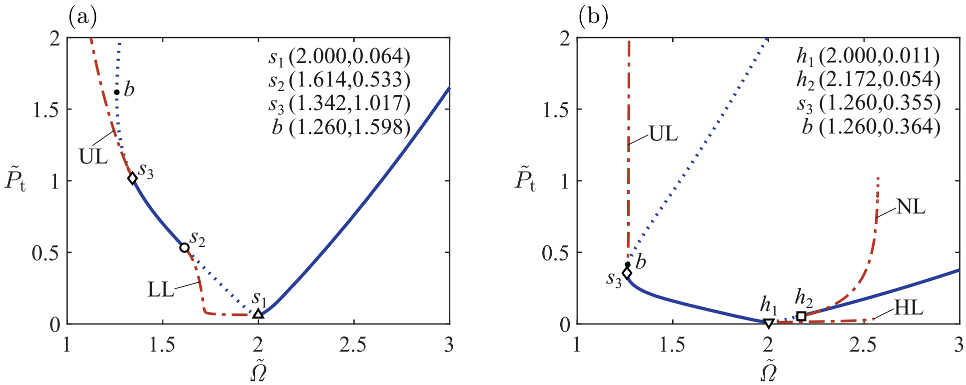

Figure 6. Loci of PD and LPC in the $\tilde{\Omega}-\tilde{P}_t$ plane with (a) $\tilde{P}_0 = 0.3$, (b) $\tilde{P}_0 = 0.85$. Solid and dotted lines denote supercritical and subcritical PD loci, respectively. The dashed–dotted line denotes LPC loci. 'UL', 'LL', 'HL' and 'NL' stand for upper softening, lower softening, hardening and neutral LPC loci, respectively.

Table 3. Bifurcation structure of various PPR peaks: $\tilde{\Omega}_{LPC}$, $\tilde{\Omega}_L$ and $\tilde{\Omega}_R$ denote the frequencies of the LPC, the left PD and the right PD; LPD and RPD denote left and right PD; 'Sub' and 'Super' denote subcritical and supercritical PD.

	number and position of LPCs		criticality of PDs	
resonance behaviour	number	position	LPD	RPD
neutral	0	NA	Super	Super
softening	1	$\tilde{\Omega}_{LPC} < \tilde{\Omega}_L$	Sub	Super
hardening	1	$\tilde{\Omega}_{LPC} > \tilde{\Omega}_R$	Super	Sub
neutral-hardening	2	$\tilde{\Omega}_{LPC1} = (\tilde{\Omega}_L, \tilde{\Omega}_R)$; $\tilde{\Omega}_{LPC2} > \tilde{\Omega}_R$	Super	Super
softening–hardening	3	$\tilde{\Omega}_{LPC1} < \tilde{\Omega}_L$; $\tilde{\Omega}_{LPC2} = (\tilde{\Omega}_L, \tilde{\Omega}_R)$; $\tilde{\Omega}_{LPC3} > \tilde{\Omega}_R$	Sub	Super

The analysis above demonstrates that each type of response behaviour corresponds to a unique bifurcation structure, characterized by the number and location of LPCs and by the criticality of the PDs; this classification is summarized in table 3. Two distinct trends emerge: (1) for lower values of $\tilde{P}_0$, increasing $\tilde{P}_t$ causes the resonance peak initially to exhibit a softening-type behaviour, then progressively lose these characteristics to become neutral-type, and subsequently recover softening characteristics, as illustrated by the case $\tilde{P}_0 = 0.3$; (2) for values of $\tilde{P}_0$ close to unity, the resonance peak initially displays a hardening-type behaviour, transitioning to neutral-hardening-type with increasing $\tilde{P}_t$, and it ultimately evolves into softening–hardening-type behaviour, as shown for $\tilde{P}_0 = 0.85$.

(ii) Two-parameter continuation in the $\tilde{\Omega}-\tilde{P}_t$ plane

The analyses above have shown that the bifurcation structure provides a clear indication of the behaviour of the resonance peak. To obtain a more complete picture of the influence of $\tilde{P}_t$ on the PPR peak, loci of LPC and PD bifurcations are computed via two-parameter continuation using $\tilde{\Omega}$ and $\tilde{P}_t$ as free parameters, while enforcing the relevant singularity conditions and fixing all other parameters. Similar to the previous section, two representative cases are considered, $\tilde{P}_0 = 0.3$ and 0.85, which have been shown above to exhibit distinctly different bifurcation structures.

For $\tilde{P}_0 = 0.3$, the PD locus exhibits a rounded 'V' shape at low $\tilde{P}_t$, with its vertex at s_1 (figure 6a). Below this threshold, no PD bifurcation occurs, corresponding to the disappearance of the PPR peak. Above s_1, the PD locus is found to split into two branches associated with the left and right PDs. Along the left branch, $\tilde{\Omega}$ decreases as $\tilde{P}_t$ increases, whereas along the right branch it increases monotonically. This produces a progressive widening of the PPR frequency span with increasing $\tilde{P}_t$.

At the vertex s_1, the first generalized period-doubling point (GPD), also termed as a degenerate PD, is detected. The positions of s_1 and subsequent GPDs are given in figure 6. The GPD is a codimension-2 bifurcation point on the PD locus where the cubic coefficient of the PD normal form vanishes. Locally, it signifies two key features: (i) the transition between supercritical and subcritical PD bifurcations, and (ii) the emergence of a locus of LPC bifurcations of period-doubled orbits, tangential to the PD locus. Around s_1, the supercritical right PD branch transitions to the subcritical left branch. From the same point, the lower softening LPC locus emanates, rapidly detaches from the PD locus, and extends towards lower $\tilde{\Omega}$. This indicates the onset of softening-type behaviour and creates a maximum frequency separation between the PD and LPC loci, $\Delta\tilde{\Omega}$, just above s_1, corresponding to the strongest softening-type behaviour. With further increase of $\tilde{P}_t$, the LPC locus curves back towards the PD locus, reducing $\Delta\tilde{\Omega}$ and hence weakening the softening effect, before reconnecting at s_2. Beyond s_2, the lower softening LPC locus terminates, leaving only the PD locus and marking a transition from softening-type to neutral-type response.

Above s_2, the left PD branch remains but switches to being supercritical. This persists until the branch passes through s_3, where the behaviour reverts to subcritical. Beyond s_3, a new upper softening LPC locus emerges, branching away from the left PD locus and extending towards lower $\tilde{\Omega}$, which signals the transition from a neutral-type back to a softening-type response. As $\tilde{P}_t$ increases further, the left PD branch reaches the ‘U-turn’ point b, then curves back with increasing $\tilde{\Omega}$. Meanwhile, the upper softening LPC locus extends towards lower $\tilde{\Omega}$, increasing $\Delta\tilde{\Omega}$ and enhancing the softening effect. In contrast with the relatively rich behaviour on the left PD branch, the right PD branch is simpler by remaining supercritical throughout above s_1 with no LPC loci observed.

As shown in figure 6b for $\tilde{P}_0 = 0.85$, the loci of PD and LPC bifurcations are organized qualitatively differently compared to the $\tilde{P}_0 = 0.3$ case. Three GPDs are detected on the PD locus: h_1, located at the minimum of the PD locus (analogous to s_1 when $\tilde{P}_0 = 0.3$); h_2, situated further along the right PD branch; s_3, located on the left PD branch, similar to the $\tilde{P}_0 = 0.3$ case. At h_1, the left PD branch, which is supercritical, connects to the right branch and becomes subcritical. From this point, a hardening LPC locus emerges, which diverges from the PD locus, and extends towards higher frequencies, indicating the onset of a hardening-type response. Although the hardening LPC locus extends to a relatively high $\tilde{P}_t$, its numerical continuation becomes challenging for large $\tilde{P}_t$ due to the small viscous damping, and thus only the branch near h_1 is shown. Upon reaching h_2, the right PD branch switches back to supercritical. From this point, the neutral LPC locus branches off and extends towards higher $\tilde{P}_t$, marking the transition from hardening-type to neutral–hardening-type behaviour. Unlike the hardening LPC locus, which lies at higher frequencies compared to the PD locus, the neutral LPC locus is positioned between the left and right PD branches.

The third codimension-2 point, s_3, is identified on the left PD branch for $\tilde{P}_t$ above h_2. Here, the supercritical left PD branch becomes subcritical and the upper softening LPC locus emerges from s_3, diverging from the left PD branch. Above s_3, the hardening, neutral and upper softening LPC loci coexist, corresponding to a softening–hardening-type resonance peak. With $\tilde{P}_t$ increasing further, the left PD branch decreases in frequency until reaching the ‘U-turn’ point b, after which it curves back with increasing $\tilde{\Omega}$; the frequency separation between the left PD branch and the upper softening LPC locus progressively widens. This curving back behaviour of the left PD branch explains the ‘U-turn’ behaviour of the left PD observed in figure 5d.

(iii) Effect of $\tilde{P}_0$ on LPC and PD loci

The analyses above have shown that different $\tilde{P}_0$ levels correspond to distinct structures of the LPC and PD loci within the $\tilde{\Omega}-\tilde{P}_t$ plane. In the current section, through fixing different $\tilde{P}_0$ values, the evolution of the LPC and PD loci is investigated to address the combined effect between $\tilde{P}_0$ and $\tilde{P}_t$ on the response behaviour. The effect of $\tilde{P}_0$ on PD loci is presented in figure 7a. With $\tilde{P}_0$ increasing, the slope of the right PD branch reduces; the ‘U-turn’ point b on the left PD branch reduces towards lower $\tilde{P}_t$; all b values occur at $\tilde{\Omega} = 1.26$, which constrains the PD loci expansion.

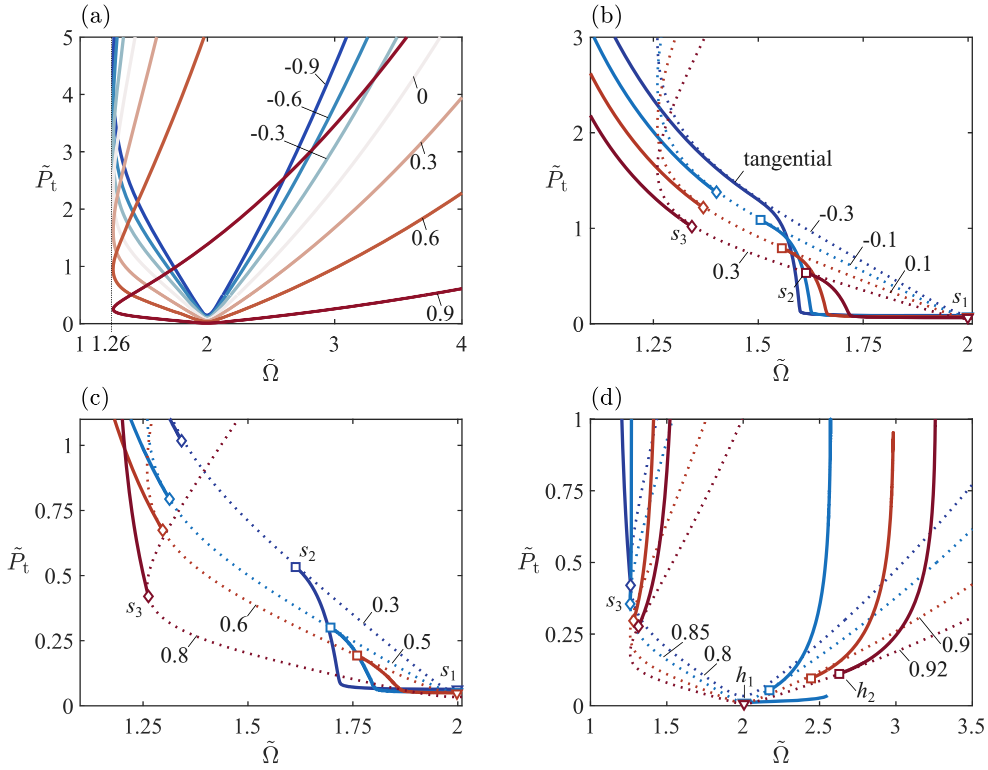

Figure 7. Loci of PD and LPC in the $\tilde{\Omega}-\tilde{P}_t$ plane with varying $\tilde{P}_0$. In (a), solid lines denote PD loci. In (b)–(d), solid lines denote LPC loci and dotted lines denote PD loci. (a) Effect of varying $\tilde{P}_0$ from −0.9 to 0.9 on PD loci; (b) effect of varying $\tilde{P}_0$ from tension (negative $\tilde{P}_0$) to compression (positive $\tilde{P}_0$) on GPDs and LPC loci; (c) effect of increasing compressive $\tilde{P}_0$ on GPDs and LPC loci; (d) effect of $\tilde{P}_0$ being close to the buckling load on GPDs and LPC loci.

Decreasing $\tilde{P}_0$ extends the lower softening LPC locus towards higher $\tilde{P}_t$ and expands the area bounded by the lower softening LPC loci and the left PD branch, see figure 7b. For $\tilde{P}_0$ being reduced from 0.3 to 0.1 and −0.1 (where negative $\tilde{P}_0$ denotes a tensile static axial load), s_1 remains at approximately constant $\tilde{\Omega}$ and shifts slightly to higher $\tilde{P}_t$ values. In contrast, both s_2 and s_3 move towards higher $\tilde{P}_t$ and lower $\tilde{\Omega}$ values, reflecting a divergence from s_1. At $\tilde{P}_0 = -0.229$, s_2 coalesces with s_3, causing both bifurcations to vanish. Consequently, the lower and upper softening LPC loci merge to form a continuous LPC locus, originating from s_1 and extending towards higher $\tilde{P}_t$ values. This indicates that, for $\tilde{P}_0 < -0.229$, only a softening-type PPR peak is achievable above s_1. An example of this configuration is illustrated in figure 7b for $\tilde{P}_0 = -0.3$.

Increasing compressive levels of $\tilde{P}_0$ produces the opposite trend: the upper softening LPC extends towards lower $\tilde{P}_t$, the lower softening LPC locus shortens and thus reduces the area bounded by the lower softening LPC loci and the left PD branch, see figure 7c. For $\tilde{P}_0$ being increased from 0.3 to 0.5 and 0.6, s_1 retains nearly constant $\tilde{\Omega}$ while shifting slightly to lower $\tilde{P}_t$ values. Meanwhile, both s_2 and s_3 shift to lower $\tilde{P}_t$ and higher $\tilde{\Omega}$ values, indicating an approach towards s_1. At $\tilde{P}_0 = 0.758$, s_2 coalesces with s_1, causing both bifurcations to vanish. In this case, the lower softening LPC locus vanishes, and thus, only the neutral-type response is expected below s_3. An illustrative example is shown in figure 7c with $\tilde{P}_0 = 0.8$.

For $\tilde{P}_0 > 0.812$, h_1 and h_2 emerge. For $\tilde{P}_0$ increasing further to 0.85, 0.9 and 0.92, see figure 7d, h_1 retains an approximately constant $\tilde{\Omega}$ while shifting slightly to lower $\tilde{P}_t$ values. Owing to the challenges of numerical solution, only a segment of the hardening LPC locus for $\tilde{P}_0 = 0.85$ is presented. Simultaneously, s_3 moves towards lower $\tilde{P}_t$ and higher $\tilde{\Omega}$ values, while h_2 drifts towards both higher $\tilde{P}_t$ and higher $\tilde{\Omega}$ values. These reflect s_3 approaching towards h_1, while h_2

diverges from h_1. The merging of s_3 and h_1 has not been observed within the pre-buckling scenario considered presently (i.e. $\tilde{P}_0 < 1$).

https://royalsocietypublishing.org/journal/rspa Proc. R. Soc. A 482: 20260072

(iv) Three-parameter continuation in the $\tilde{P}_0$—$\tilde{P}_t$—$\tilde{\Omega}$ space

The analyses above have shown that, within the $\tilde{\Omega}$–$\tilde{P}_t$ plane, GPDs appear along the PD loci, indicating changes in their criticality; each GPD corresponds to the onset of a specific LPC locus. Consequently, for a given $\tilde{P}_0$, these GPDs partition $\tilde{P}_t$ into several ranges associated with distinct bifurcation structures—defined by the number and location of LPC loci and the criticality of both PD branches—which, in turn, correspond to different resonance behaviours, as summarized in table 3. As $\tilde{P}_0$ varies, the GPDs move and interact, reflecting the evolution of these $\tilde{P}_t$ ranges. To capture the combined influence of $\tilde{P}_0$ and $\tilde{P}_t$ on the resonance behaviour, it is, therefore, necessary to investigate the GPD loci within the full $\tilde{P}_0$–$\tilde{P}_t$–$\tilde{\Omega}$ space.

The loci of GPDs are evaluated by allowing $\tilde{P}_0$, $\tilde{P}_t$ and $\tilde{\Omega}$ to vary freely, while enforcing both the non-trivial negative one Floquet multiplier condition (i.e. the PD condition) and the additional degeneracy condition that the cubic term in the PD normal form vanishes. The resulting loci form three-dimensional curves in the parameter space, with their projections, respectively, onto the $\tilde{P}_0$–$\tilde{P}_t$ plane shown in figure 8a. In total, five distinct GPD loci are detected, corresponding to s_1, s_2, s_3, h_1 and h_2 from the previous section. These loci partition the parameter space into regions of distinct resonance behaviour, while their intersections signal the presence of possible higher codimension bifurcations.

The loci of s_1 and s_2 merge and terminate at $(\tilde{P}_0, \tilde{P}_t, \tilde{\Omega}) = (0.758, 0.042, 1.964)$. At this intersection, a higher-order degeneracy, here termed a degenerate GPD ('dGPD', denoted as d_1), is detected, corresponding to the additional condition that the quintic coefficient in the PD normal form also vanishes. This codimension-3 bifurcation marks the disappearance of both s_1 and s_2, together with the disappearance of the lower softening LPC loci emanating from them. A second dGPD (d_2) is found at $(0.812, 0.020, 2.028)$, associated with the merging of the h_1 and h_2 loci. This higher-order bifurcation corresponds to the simultaneous creation of hardening and neutral LPC loci, and may, therefore, be interpreted as the onset of hardening behaviour within the system.

The loci of s_2 and s_3 also merge and vanish at $(-0.229, 1.376, 1.450)$. This point is algebraically a GPD, i.e. it satisfies the condition of a non-trivial negative one multiplier together with the vanishing cubic coefficient of the PD normal form. However, the usual feature of a GPD is absent: the criticality of the PD does not change across this point and no period-doubled LPC branch emanates. Instead, this point marks the formation of a continuous LPC locus through the merging of the lower and upper softening loci, accompanied by tangency and eventual detachment of this locus from the PD loci. Therefore, it is classified as a pseudo-GPD (denoted p), i.e. an algebraic GPD without the associated change in the dynamics.

Building on the analyses presented in the previous sections, the resonance behaviour can be classified as follows. The domain enclosed from below by the joint s_1, s_2 and s_3 loci (the 'yellow' area in figure 8a) corresponds to the softening-type resonance for $\tilde{P}_0 < d_2(\tilde{P}_0)$ (where '$d_2(\tilde{P}_0)$' denotes the $\tilde{P}_0$ value of d_2). The wedge-shaped region bounded by the h_1 and h_2 loci (the 'pink' area in figure 8a) corresponds to the hardening-type resonance. The remaining regions of the parameter space are divided into three areas: (1) for $\tilde{P}_0 < d_2(\tilde{P}_0)$, the neutral-type behaviour is expected (the 'cyan' area in figure 8a); (2) the area enclosed by the s_3 and h_2 loci with $\tilde{P}_0 > d_2(\tilde{P}_0)$ corresponds to the neutral–hardening-type behaviour (the 'lavender' area in figure 8a); and (3) the area above the s_3 locus with $\tilde{P}_0 > d_2(\tilde{P}_0)$ corresponds to the softening–hardening-type behaviour (the 'green' area in figure 8a). FE simulations have been conducted to verify these behavioural regions and present good agreement with the analytical predictions with the FE frequency-response results presented in §S2 of the electronic supplementary material. It is noteworthy that the FE simulations exhibit neutral-type and softening-type responses within the analytically predicted neutral–hardening-type and softening–hardening-type parameter regions, respectively. This discrepancy is attributed to the fact that the hardening behaviour in these regions occurs only

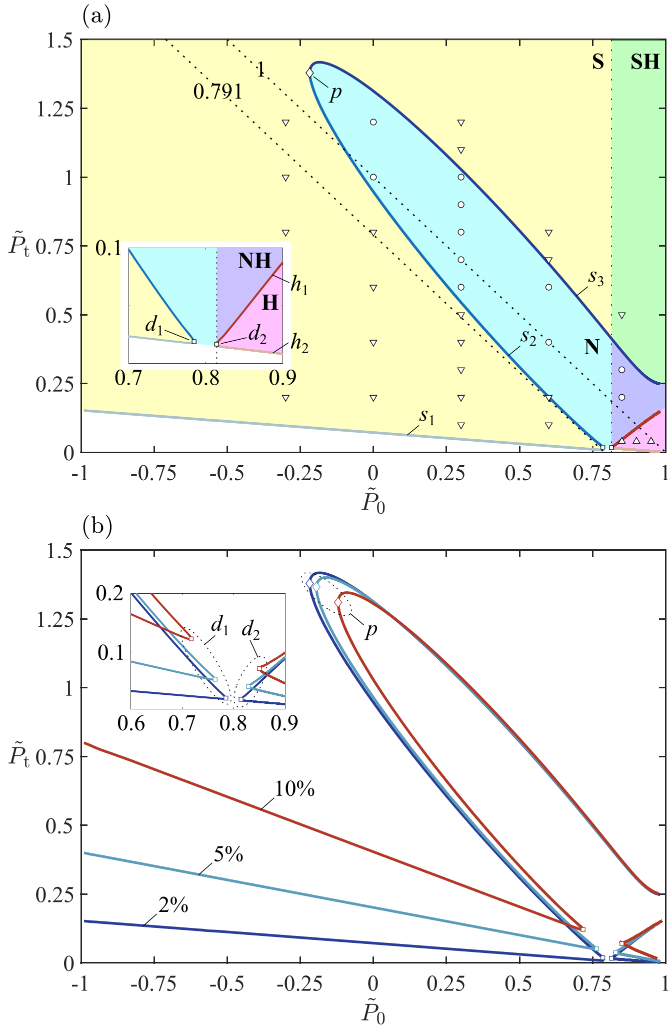

Figure 8. (a) Projection of GPD loci onto the $\tilde{P}_0$—$\tilde{P}_t$ plane. Dotted lines denote $\tilde{P}_0 + \tilde{P}_t$ equal to 1 and 0.791; d_1 and d_2 are degenerate GPDs and p is a pseudo-GPD. Symbols: '○', '▽' and '△' denote neutral, softening and hardening resonance obtained by FE simulations; 'N', 'S', 'H', 'NH' and 'SH' denote the parametric regions of neutral, softening, hardening, neutral-hardening and softening–hardening behaviour, respectively. (b) Effect of damping ratio ξ on GPD loci.

at very large response amplitudes ($\tilde{Q} > 0.3$), where achieving steady-state convergence in the FE simulations becomes increasingly challenging.

Notably, the s_3 locus lies entirely above the boundary $\tilde{P}_0 + \tilde{P}_t = 1$, indicating that this branch corresponds to behaviour under severe axial loading within the post-buckling range for at least some of the time within a cycle. Comparison with the free-undamped response highlights the role of parametric excitation. In the absence of excitation, the softening–hardening transition occurs at $\tilde{P}_0 = 0.791$. With excitation, the corresponding condition $\tilde{P}_0 + \tilde{P}_t = 0.791$ serves only as an approximate boundary. For $\tilde{P}_0 = (0.5, 0.8)$, this approximation remains accurate; however, for $\tilde{P}_0 < 0.5$, increasing divergence is observed as the s_2 locus deviates significantly from the line $\tilde{P}_0 + \tilde{P}_t = 0.791$. In addition, for $\tilde{P}_0 > 0.8$, more complex resonance behaviour is expected instead of pure hardening-type behaviour.

The effect of damping on the GPD loci is shown in figure 8b. Increasing ξ leads to an increase in the slope magnitudes of the s_1 and h_1 loci, while having only a minor influence on the remaining loci. As a result, higher damping raises the $\tilde{P}_t$ threshold for the onset of PPR resonance and shrinks the parameter regions corresponding to the softening-type and the hardening-type responses within the $\tilde{P}_0-\tilde{P}_t$ space. Moreover, increasing ξ causes a greater separation between d_1 and d_2. It is, therefore, postulated that for the undamped case, d_1 and d_2 would in fact coalesce.

7. Concluding remarks

The present study has investigated the nonlinear resonance characteristics of a pre-buckled strut subjected to finite static axial loading and harmonic parametric excitation. The governing equation of the simply supported slender strut was derived under the condition of inextensibility, truncated to cubic order and discretized primarily using the first buckling mode. The steady-state response was investigated extensively via numerical continuation techniques and verified with FE simulations. The backbone curve of the strut obtained through applying the harmonic balance method on the free-undamped system was shown to be significantly influenced by the static axial load level P_0. A stronger softening effect was expected in tension or at low compression levels of P_0, whereas a weaker softening effect occurred at higher compressive levels. A hardening-type backbone curve emerged when P_0 exceeds approximately 80% of the critical buckling load.

The analysis then focused on the frequency–response function in the neighbourhood of the principal parametric resonance peak, which is widely adopted in energy harvesting and signal detection systems, owing to its wide bandwidth and large deflections under small excitations. The resonance peak was classified as neutral, softening, hardening, neutral–hardening, or softening–hardening, according to the trend of the resonance curve and the corresponding bifurcation structure, namely the criticality of period-doubling bifurcation points (PDs) alongside the number and positions of limit point bifurcations of cycles (LPCs). Two-parameter continuations of the PD and LPC loci were performed to identify the parameter regions associated with the principal parametric resonance and to reveal the influence of $\tilde{P}_t$ on the response type; generalized PDs (GPDs) were found along the PD loci from which LPC loci of doubled-period emerged and the criticality of PD transitioned. Consequently, they acted as indicators marking the transitions in resonance behaviour. Extending the analysis by determining GPD loci identified five regions, each corresponding to one of the five types of resonance behaviour. This resonance map provides essential insight for the design of structural isolation, energy harvesting and signal detection systems, where a judicious choice of dynamical characteristics can enhance performance over a wider range of excitation frequencies and amplitudes. A natural extension of the present work would be the relaxation of the linear elasticity assumption to incorporate more general viscoelastic or hysteretic behaviour, particularly for polymer-based benchmark structures.

Data accessibility. The data supporting this study are available at: [43].

The data are provided in the electronic supplementary material [44].

Declaration of AI use. We have not used AI-assisted technologies in creating this article.

Authors' contributions. Y.C.: formal analysis, investigation, validation, visualization, writing—original draft; M.A.W.: conceptualization, investigation, methodology, supervision, writing—review and editing; C.M.C.: conceptualization, investigation, methodology, supervision, writing—review and editing.

All authors gave final approval for publication and agreed to be held accountable for the work performed therein.

Conflict of interest declaration. We declare we have no competing interests.

Funding. The lead author is supported by the Skempton scholarship awarded by the Department of Civil and Environmental Engineering, Imperial College London.

References

1. Thompson JMT, Hunt GW. 1973 *A general theory of elastic stability*. London: Wiley.
2. Plaut RH, Sidbury JE, Virgin LN. 2005 Analysis of buckled and pre-bent fixed-end columns used as vibration isolators. *J. Sound Vib.* **283**, 1216–1228. (doi:10.1016/j.jsv.2004.07.029)

3. Liu C, Zhao R, Yu K, Lee HP, Liao B. 2021 A quasi-zero-stiffness device capable of vibration isolation and energy harvesting using piezoelectric buckled beams. *Energy* **233**, 121146. (doi:10.1016/j.energy.2021.121146)
4. Fang S, Peng H, Zhang C, Lai Z, Zhou S, Zhu R, Liao WH, Inman DJ. 2024 Synchronous and asynchronous vibration suppression and energy harvesting techniques: principles, methods and applications. *Eng. Struct.* **321**, 118994. (doi:10.1016/j.engstruct.2024.118994)
5. Daqaq MF, Stabler C, Qaroush Y, Seuaciuc-Osório T. 2008 Investigation of power harvesting via parametric excitations. *J. Intell. Mater. Syst. Struct.* **20**, 545–557. (doi:10.1177/1045389x08100978)
6. Bekele A, Wadee MA, Phillips ATM. 2023 Enhancing energy absorption through sequential instabilities in mechanical metamaterials. *R. Soc. Open Sci.* **10**, 230762. (doi:10.1098/rsos.230762)
7. Hunt GW, Peletier MA, Champneys AR, Woods PD, Wadee MA, Budd CJ, Lord GJ. 2000 Cellular buckling in long structures. *Nonlinear Dyn.* **21**, 3–29. (doi:10.1023/A:1008398006403)
8. Wadee MA, Farsi M. 2014 Cellular buckling in stiffened plates. *Proc. R. Soc. A* **470**, 20140094. (doi:10.1098/rspa.2014.0094)
9. Dykstra DMJ, Lenting C, Masurier A, Coulais C. 2023 Buckling metamaterials for extreme vibration damping. *Adv. Mater.* **35**, 202301747. (doi:10.1002/adma.202301747)
10. Coaquira JC, Cardoso DCT, Gonçalves PB, Orlando D. 2020 Parametric instability and nonlinear oscillations of an FRP channel section column under axial load. *Nonlinear Dyn.* **103**, 3557–3580. (doi:10.1007/s11071-020-05663-x)
11. Bolotin VV. 1962 *Dynamic stability of elastic systems*. San-Francisco: Holden-Day. (doi:10.21236/AD0295758)
12. Crespo da Silva MRM, Glynn CC. 1978 Nonlinear flexural-flexural-torsional dynamics of inextensional beams. I. Equations of motion. *J. Struct. Mech.* **6**, 437–448. (doi:10.1080/03601217808907348)
13. Nayfeh AH, Pai PF. 2004 *Linear and nonlinear structural mechanics*. Weinheim: Wiley-VCH. (doi:10.1002/9783527617562)
14. Luongo A, Zulli D. 2013 *Mathematical models of beams and cables*. ISTE. Hoboken: Wiley, includes bibliographical references and index. (doi:10.1002/9781118577554)
15. Lacarbonara W, Yabuno H. 2006 Refined models of elastic beams undergoing large in-plane motions: Theory and experiment. *Int. J. Solids Struct.* **43**, 5066–5084. (doi:10.1016/j.ijsolstr.2005.07.018)
16. Emam SA, Nayfeh AH. 2004 On the nonlinear dynamics of a buckled beam subjected to a primary-resonance excitation. *Nonlinear Dyn.* **35**, 1–17. (doi:10.1023/b:nody.0000017466.71383.d5)
17. Abou-Rayan AM, Nayfeh AH, Mook DT, Nayfeh MA. 1993 Nonlinear response of a parametrically excited buckled beam. *Nonlinear Dyn.* **4**, 499–525. (doi:10.1007/bf00053693)
18. Lenci S, Rega G. 2016 Axial–transversal coupling in the free nonlinear vibrations of Timoshenko beams with arbitrary slenderness and axial boundary conditions. *Proc. R. Soc. A* **472**, 20160057. (doi:10.1098/rspa.2016.0057)
19. Atluri S. 1973 Nonlinear vibrations of a hinged beam including nonlinear inertia effects. *J. Appl. Mech.* **40**, 121–126. (doi:10.1115/1.3422909)
20. Mettler E. 1962 *Handbook of engineering mechanics*. New York: McGraw-Hill.
21. Kibach H, Ture S, Lamarque CH. 2025 Free vibrations of an elastica around its post-buckled configurations. *Int. J. Non-Linear Mech.* **179**, 105250. (doi:10.1016/j.ijnonlinmec.2025.105250)
22. Mallon NJ, Fey RHB, Nijmeijer H. 2006 Dynamic stability of a base-excited thin beam with top mass. In *Applied Mechanics IMECE2006*, pp. 221–230. ASMEDC. (doi:10.1115/imece2006-13148).
23. Nayfeh AH, Pai PF. 1989 Non-linear non-planar parametric responses of an inextensional beam. *Int. J. Non-Linear Mech.* **24**, 139–158. (doi:10.1016/0020-7462(89)90005-x)
24. Latalski J, Kloda L, Dubicka-Nowak J. 2026 Nonlinear dynamics of an axially preloaded hinged–hinged planar beam—experimental insights, finite element modal analysis and analytical modeling. *J. Sound Vib.* **620**, 119434. (doi:10.1016/j.jsv.2025.119434)
25. Kloda L, Lenci S, Warminski J. 2020 Hardening vs. softening dichotomy of a hinged-simply supported beam with one end axial linear spring: experimental and numerical studies. *Int. J. Mech. Sci.* **178**, 105588. (doi:10.1016/j.ijmecsci.2020.105588)
26. Fung RF. 1997 The effect of non-linear inertia on the steady state response of a beam system subjected to combined excitations. *J. Sound Vib.* **203**, 373–387. (doi:10.1006/jsvi.1996.0924)

27. Evensen HA, Evan-Iwanowski RM. 1966 Effects of longitudinal inertia upon the parametric response of elastic columns. *J. Appl. Mech.* **33**, 141–148. (doi:10.1115/1.3624971)
28. Köllner A, Lüer N. 2025 A path-following approach for quasi-static structural and material instability phenomena. *Comput. Meth. Appl. Mech. Eng.* **436**, 117704. (doi:10.1016/j.cma.2024.117704)
29. Dhooge A, Govaerts W, Kuznetsov YA. 2003 MATCONT: A MATLAB package for numerical bifurcation analysis of ODEs. *ACM Trans. Math. Softw.* **29**, 141–164. (doi:10.1145/779359.779362)
30. ABAQUS. 2021 *ABAQUS user guide*. Dassault Systèmes Simulia.
31. Mathieu E. 1868 Mémoire sur le mouvement vibratoire d'une membrane de forme elliptique. *J. Math. Pures Appl.* **13**, 137–203.
32. Nayfeh AH. 2011 *Introduction to perturbation techniques*. Weinheim: Wiley-VCH.
33. Dashtkar A, Hadavinia H, Barros-Rodriguez J, Williams NA, Turner M, Vahid S. 2021 Quantifying damping coefficient and attenuation at different frequencies for graphene modified polyurethane by drop ball test. *Polym. Test.* **100**, 107267. (doi:10.1016/j.polymertesting.2021.107267)
34. MATLAB. 2023 *version 9.14.0 (R2023a)*. Natick, Massachusetts: The MathWorks Inc.
35. Riks E. 1979 An incremental approach to the solution of snapping and buckling problems. *Int. J. Solids Struct.* **15**, 529–551. (doi:10.1016/0020-7683(79)90081-7)
36. Kibriya L, Málaga-Chuquitaype C, Kashani M. 2020 Buckling-enabled composite bracing for damage-avoidance rocking structures. *Int. J. Mech. Sci.* **170**, 105359. (doi:10.1016/j.ijmecsci.2019.105359)
37. Kibriya L, Málaga-Chuquitaype C, Kashani M, Alexander N. 2018 Nonlinear dynamics of self-centring rocking steel frames using finite element models. *Soil Dyn. Earthq. Eng.* **115**, 826–837. (doi:10.1016/j.soildyn.2018.09.036)
38. Virgin LN. 2012 *Vibration of axially-loaded structures*. Cambridge: Cambridge University Press.
39. Kovacic I, Rand R, Mohamed Sah S. 2018 Mathieu's equation and its generalizations: overview of stability charts and their features. *Appl. Mech. Rev.* **70**, 020802. (doi:10.1115/1.4039144)
40. Nayfeh AH. 2008 *Nonlinear oscillations*. New York: Wiley.
41. Zavodney LD, Nayfeh AH, Sanchez NE. 1989 The response of a single-degree-of-freedom system with quadratic and cubic non-linearities to a principal parametric resonance. *J. Sound Vib.* **129**, 417–442. (doi:10.1016/0022-460x(89)90433-1)
42. Shibata A, Ohishi S, Yabuno H. 2015 Passive method for controlling the nonlinear characteristics in a parametrically excited hinged-hinged beam by the addition of a linear spring. *J. Sound Vib.* **350**, 111–122. (doi:10.1016/j.jsv.2015.03.055)
43. Cheng Y, Wadee MA, Málaga-Chuquitaype C. 2026 Shared Data and Supplementary Material of 'Nonlinear Resonance Characterization of Parametrically Excited Pre-buckled Elastic Struts'. See https://github.com/CMalagaC/Parametrically_Excited_Pre-buckled_Strut_Paper/tree/main. (doi:10.5281/zenodo.19701820).
44. Cheng Y, Ahmer Wadee M, Málaga-Chuquitaype C. 2026 Nonlinear resonance characterization of parametrically excited pre-buckled elastic struts. Figshare. (doi:10.6084/m9.figshare.c.8519930)